Journal Pre-proof

Fatigue phase-field damage modeling of rubber using viscous dissipation: Crack nucleation and propagation

Pascal J. Loew, Bernhard Peters, Lars A.A. Beex

PII: S0167-6636(19)30640-4
DOI: https://doi.org/10.1016/j.mechmat.2019.103282
Reference: MECMAT 103282

To appear in: *Mechanics of Materials*

Received date: 26 July 2019
Revised date: 9 December 2019
Accepted date: 11 December 2019

Please cite this article as: Pascal J. Loew, Bernhard Peters, Lars A.A. Beex, Fatigue phase-field damage modeling of rubber using viscous dissipation: Crack nucleation and propagation, *Mechanics of Materials* (2019), doi: https://doi.org/10.1016/j.mechmat.2019.103282

Highlights

- Extending a finite strain phase-field damage model to accurately predict fatigue failure
- Using the degradation and crack density function acc. Wu et al. 2018 to present length scale independent global reaction forces
- Predicting crack nucleation and crack growth in 2D
- Validating the model with experimental data for fracture and fatigue

Fatigue phase-field damage modeling of rubber using viscous dissipation: Crack nucleation and propagation

Pascal J. Loew[a,b,*], Bernhard Peters[a], Lars A.A. Beex[a]

[a] *Faculté des Sciences, de la Technologie et de la Communication, Université du Luxembourg*
[b] *SISTO Armaturen S.A., Echternach*

Abstract

By regularizing sharp cracks within a pure continuum setting, phase-damage models offer the ability to capture crack nucleation as well as crack propagation. Crack branching and coalescence can furthermore be described without any additional efforts, as geometrical descriptions of the cracks are not required. In this contribution, we extend our previous phase-field model for rate-dependent fracture of rubbers in a finite strain setting (Loew et al. 2019) to describe damage under cyclic loading. The model is derived from the balance of mechanical energy and introduces a fatigue damage source as a function of the accumulated viscous dissipation under cyclic loading. We use uniaxial cyclic tension to present the influence of the fatigue material parameters and to confirm the model's energy balance. The parameters are subsequently identified using monotonic and cyclic experiments of a plane stress nature. Finally, the model is validated by separate experiments, which demonstrate that the model accurately predicts (fatigue) crack nucleation as well as propagation.

Keywords: Phase-field, fatigue, damage, rubber, rate-dependent

*Corresponding author
Email address: loew.pascal@gmail.com (Pascal J. Loew)

1. Introduction

Virtual prototypes can be used to reduce the financial burden of physical prototypes in design processes. They also allow more designs to be evaluated but require accurate mechanical models to describe the three stages of (fatigue) failure: crack initiation, crack propagation and final fracture.

The lifetime of rubber parts is affected by many factors ([19], [20]), which can be subdivided into four classes: mechanical load history, environmental conditions (such as temperature), rubber formulation and constitutive behavior [20]. This contribution focuses on the mechanical load history and constitutive behavior. Hence, we test one rubber compound and ignore temperature differences and chemical aging.

Several fatigue damage models for rubber have been published: [31] presented a continuum damage model and defined the fatigue life as a function of the strain amplitude. Multi-axial loading was considered by [4], who used the cracking energy density criterion of [18]. [11] and [25] extended the theory to thermo-viscoelastic solids to describe self-heating under cycling loading. All these continuum damage models show a mesh sensitivity [27]. Therefore, [26] presented a gradient-enhanced fatigue damage model for rubber which is mesh independent. A disadvantage of traditional gradient enhanced damage models is spurious damage growth caused by large deformation in damaged elements. This results in a large diffused process zone at complete failure [28][1].

Similar to gradient enhanced damage models, phase-field damage models for fracture ([6], [21], [23]) treat the sharp discontinuities of cracks in a continuous manner by introducing a finite damage zone, governed by a length scale parameter. Consequently, they are able to handle crack propagation, branching and coalescence. The extension to finite strains and rubber was first published in [22], while [16] presented a rate-dependent phase-field damage model for rubbers.

Gradient-enhanced and phase-field damage models are similar [9], as they both rely on a length scale parameter to produce mesh insensitive results. However,

only phase-field damage models do not show the mentioned spurious damage growth, since the damage driving force vanishes for a complete loss of the stiffness [9].

To the best of the authors' knowledge, [3] was the first to consider fatigue damage in a phase-field model by introducing a fatigue history variable in the Ginzburg-Landau equation. [7] additionally introduced damage caused by aging, while [5] defined the internal fatigue history variable with a differential constitutive law to be found. [2] used a different approach and reduced the fracture toughness with cyclic loading. All these contributions show promising results for small strains in one-dimensional settings. Our model is similar to the fatigue model of [3] as we also introduce a fatigue history variable. The differences are, however, that we start the derivation from the balance of mechanical energy, define a fatigue history variable based on the viscous dissipation and allow for finite strains.

The length scale can be interpreted as a material parameter that controls the process zone in which damage occurs. It also affects the material strength in practice, i.e. the stress required to nucleate a crack [30]. [16] has shown that incorrect length scale parameters are identified if the identification is only based on the global mechanical response. To overcome this issue, local strain measurements should be included in the identification process. Recently, [33] proposed a phase-field damage model for linear elastic materials in which the length scale does not affect the global mechanical response, but merely the process zone.

Although the main objective of this work is the presentation of a fatigue phase-field damage model for rubber, this contribution combines the following novelties:

- We use the degradation function and crack density function of [33] and show that this extension also leads for finite strains and a visco-hyperelastic material to a global force response, which is not affected by the length scale parameter.
- Applying a cyclic load to the rate-dependent phase-field damage model of

[16], we show that this model describes fatigue damage but yields poor accuracy.

- Therefore, we propose an extension of our previous constitutive model [16] so that fatigue damage under cyclic loading can accurately be described. This framework also works with rate-independent materials.
- We experimentally identify all material parameters: the bulk parameters, the fracture parameters for monotonic loading and the fatigue fracture parameters for cyclic loading.
- Crack nucleation as well as crack propagation can be accurately predicted, which is presented using independent validation experiments. This is, to the best of the authors' knowledge, the first time a phase-field damage model for rubber matches uniaxial tensile test data.
- The fatigue damage model is able to predict Woehler lines and the Paris fatigue crack growth law.

The paper is organized as follows: In Section 2, we derive the generalized fatigue phase-field damage model. Section 3 presents the numerical and experimental results for monotonic loading, while the results for cyclic loading are shown in Section 4. We conclude the contribution in Section 5.
In this work, we denote scalars by lowercase and capital letters (a and A), vectors by bold, lowercase letters ($\mathbf{a}$) and second-order tensors by bold capitals ($\mathbf{A}$).

[1]Recent gradient enhanced damage approaches are able to describe sharp damage profiles [28].

2. Fatigue phase-field damage model

In this section, we derive our fatigue phase-field damage model for a body Ω_0 in the reference configuration with its external boundary denoted by $\partial\Omega_0$. We start by defining a scalar damage variable $d \in [0, 1]$ so that $d = 1$ on an internal discontinuity Γ_0 and $d = 0$ on $\Omega_0 \setminus \Gamma_0$ (Fig. 1 a)).

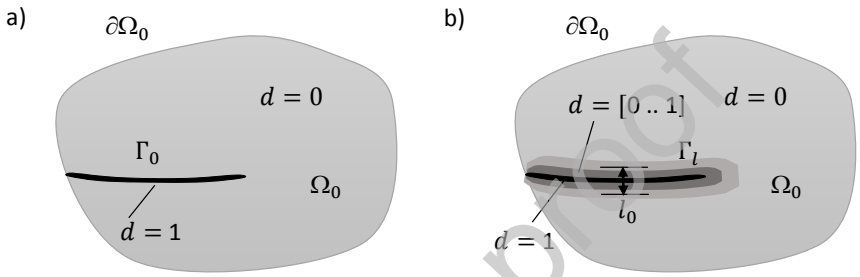

Figure 1: In a phase-field damage model, a sharp crack Γ_0 (a) is approximated with a crack surface Γ_l (b), the size of which is controlled by the length scale l_0.

The motion and deformation of the body are described by displacement $\mathbf{u}$, deformation gradient $\mathbf{F} = \mathbf{I} + \nabla_0 \mathbf{u}$ and Green's strain tensor $\mathbf{E} = 1/2(\mathbf{F}^T \cdot \mathbf{F} - \mathbf{I})$. $\mathbf{I}$ denotes the unit tensor and spatial derivatives associated with the reference configuration are denoted by $\partial \cdot / \partial \mathbf{X} = \nabla_0(\cdot)$. The balance of mechanical energy requires:

$$\dot{E} + \dot{D} = \dot{P}^{ext}, \tag{1}$$

where $\dot{E}$, $\dot{D}$ and $\dot{P}^{ext}$ denote the internally stored and dissipated energy and the externally supplied energy per time unit, respectively.
The internally stored energy in the bulk reads:

$$E = \int_{\Omega_0 \setminus \Gamma_0} \psi^{bulk} dV = \int_{\Omega_0} g_d \psi^{bulk} dV, \tag{2}$$

where we have introduced the degradation function $g_d = g_d(d)$ and the strain energy density ψ^{bulk}. The degradation function controls the mechanical re-

sponse with respect to the virgin (i.e. undamaged) state. We use a generalized degradation function, which was recently proposed in [32] and [33]:

$$g_d = \frac{(1-d)^2}{(1-d)^2 + ad(1-\frac{1}{2}d)}. \tag{3}$$

The advantage of this generalized degradation function is that the global mechanical response can be made independent of the length scale. For this, the material parameter a must be related to the selected length scale l_0 [33].
Rate-dependent effects are, as in [16], incorporated by splitting the strain energy density ψ^{bulk} into an elastic and viscous contribution:

$$\psi^{bulk} = \psi^{elas}(\mathbf{F}) + \psi^{visc}(\mathbf{F}, \Phi_\alpha). \tag{4}$$

Φ_α denotes an internal strain-like tensor, measuring the dissipation in the bulk. Assuming a material model based on m Maxwell elements, Φ_α can be considered as the 3D extension of the 1D strain γ_α in a dashpot (see Fig. 2).

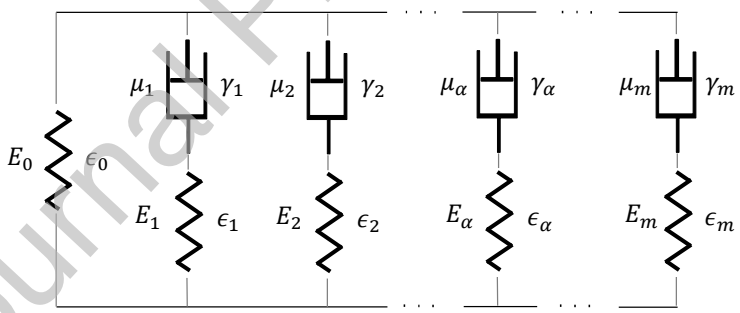

Figure 2: Schematic of a generalized Maxwell model with m spring-dashpot elements. E_α and ϵ_α denote the stiffness and strain in the spring, while μ_α and γ_α denote the viscosity and the strain in the dashpot.

The first Piola-Kirchhoff stress can consequently be expressed as follows:

$$\begin{aligned} \mathbf{P} &= \frac{\partial \psi}{\partial \mathbf{F}} = g_d \frac{\partial \psi^{bulk}}{\partial \mathbf{F}} \\ &= g_d \left(\frac{\partial \psi^{elas}}{\partial \mathbf{F}} + \sum_{\alpha=1}^{m} \frac{\partial \psi_\alpha^{vis}}{\partial \mathbf{F}} \right) \\ &= g_d \left(\mathbf{P}^\infty + \sum_{\alpha=1}^{m} \mathbf{Q}_\alpha \right). \end{aligned} \tag{5}$$

$\mathbf{P}^\infty$ denotes the time-infinity stress and $\mathbf{Q}_\alpha$ denote the non-equilibrium stresses. The rate of dissipation is attributed to three dissipative phenomena and can therefore be expressed as[2]:

$$\dot{D} = \dot{D}^{visc} + \dot{D}^{crack} + \dot{D}^{crack,visc}, \tag{6}$$

where $\dot{D}^{visc}$, $\dot{D}^{crack}$ and $\dot{D}^{crack,visc}$ denote the rate of dissipation due to the viscosity of the bulk, the rate of dissipation due to crack growth and rate-dependent crack growth dissipation, respectively.

The energy dissipated by crack growth reads:

$$D^{crack} = \int_{\Gamma_0} G_c \, dA, \tag{7}$$

where G_c denotes the energy dissipated by the formation of a unit crack area. To avoid integrating over the fractured surface Γ_0 and a sharp discontinuity, we approximate $\Gamma_0 \approx \Gamma_l = \int_{\Omega_0} \gamma_l \, dV$, with the crack density function $\gamma_l = \gamma_l(d, l_0)$ [6]. The width of the damage zone is controlled by the length scale l_0 (see Fig. 1 b)). Thus, multiplying Eq. (7) with γ_l, we can change the integration to a volume integral over the domain Ω_0:

$$D^{crack} = \int_{\Omega_0} G_c \gamma_l \, dV. \tag{8}$$

[2]For the definition of $\dot{D}^{visc}$ and $\dot{D}^{crack,visc}$, we refer to Appendix A or our previous publication [16].

We furthermore use the following crack density function [32]:

$$\gamma_l = \frac{1}{c_0}\left[\frac{1}{l_0}w + l_0\left(\nabla_0 d \cdot \nabla_0 d\right)\right], \tag{9}$$

where w denotes a geometric crack function characterizing the homogeneous evolution of the phase-field d and c_0 denotes a scaling parameter to ensure $\Gamma_0 = \Gamma_l$ for $l_0 \to 0$. The geometric crack function $w = w(d) \in [0, 1]$ must satisfy $w(d = 0) = 0$ and $w(d = 1) = 1$. As in [33], we set $w = 2d - d^2$, which yields $c_0 = 4\int_0^1 \sqrt{w(\delta)}d\delta = \pi$.

An extension to a generalized fatigue phase-field damage model is achieved by introducing $\dot{R}$[3]:

$$\dot{E} + \dot{D} = \dot{P}^{ext} + \dot{R}. \tag{10}$$

$\dot{R}$ can be interpreted as the energetic contribution of an extrinsic volumetric micro-force triggering the fatigue damage growth. Processes on a smaller scale feed this extrinsic micro-force. The relations for $\dot{E}$, $\dot{D}$ and $\dot{P}^{ext}$ are discussed in more detail in Appendix A, while $\dot{R}$ is presented in the following subsection. By inserting the relations for $\dot{E}$, $\dot{D}$, $\dot{P}^{ext}$ and $\dot{R}$ in Eq. (10), we can extract the governing equations.

2.1. Fatigue damage source

Fatigue damage is assumed to be equivalent to the formation of micro-cracks, which occur for small cyclic loads. These micro-cracks coalesce under cyclic loading and appear as damage d at the macroscale (see Fig. 3). We describe this micro-crack growth with a history variable H, so that the micro-crack formation and coalescence with each cycle is equal to the increase of H. The more micro-cracks have been formed (or the higher the value of H), the more likely macro-crack growth.

$\dot{R} = \dot{R}(H)$ is the energetic fatigue contribution to the macroscopic mechanical

[3]The fatigue framework could alternatively be derived with a balance law for micro-forces as the basis, first introduced by [12] and later used for phase-field damage models by [5].

energy balance (Eq. 10), linking the micro-cracks growth (H) to the macro-crack growth (d). We assume that micro-cracks only influence the macroscale when they have coalesced to a macro-crack. Therefore, $\dot{R}$ only contributes to the energy balance in case of damage growth ($\dot{d} \geq 0$) and we define:

$$\dot{R} = \int_{\Omega_0} H\dot{d}\, dV. \tag{11}$$

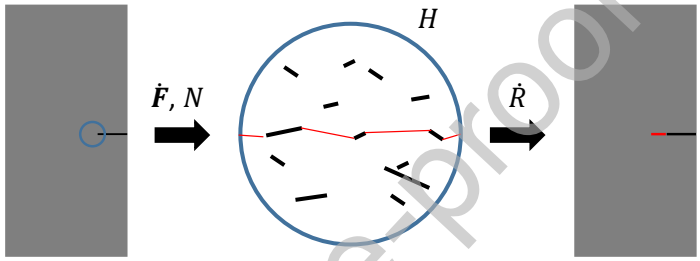

Figure 3: Schematic of micro-crack growth due to fatigue: Applying a cyclic load (characterized by N cycles and rate of deformation gradient tensor $\dot{\mathbf{F}}$) results in the formation and growth of micro-cracks (quantified by H) in regions with high stress concentrations. The coupling between micro-crack evolution and macroscale damage is established via $\dot{R}$.

The amount of micro-cracks $H = f(h)$ depends on a load history-dependent variable h, which has to be specified. Further, we introduce two fatigue damage material parameters ζ_d and ζ_e, and a fatigue degradation function $g_f = g_f(d)$ so that:

$$H = g_f \zeta_d h^{\zeta_e}. \tag{12}$$

The fatigue degradation function $g_f = g_f(d)$ ensures that micro-cracks only form in regions without a macro-crack and therefore must fulfill[4]:

$$\begin{aligned} g_f(d=0) &= 1 \\ g_f(d=1) &= 0. \end{aligned} \tag{13}$$

In the gradient enhanced damage model of [26], the load history-dependent variable is a function of the strain energy density, i.e. $h = f(\psi^{elas})$. The fatigue phase-field damage models of [3] and [5] use $h = h(\psi^{bulk} = \int \mathbf{P} : \dot{\mathbf{F}} dt,)$, while [2] sets $h = f(\epsilon, \dot{\epsilon})$. We see micro-crack formation as a dissipative mechanism and therefore propose a load history variable depending on the energy dissipated under cyclic loading in the bulk:

$$h = \psi^{visc} = \sum_{\alpha=1}^{m} \int \mathbf{Q}_\alpha : \dot{\mathbf{F}} dt, \tag{14}$$

i.e. the hysteresis. The advantage of an energetic fatigue failure criterion for rubbers over a maximum stress or strain criterion was shown by several studies ([1], [17]). For simplicity, we set $g_f = -\partial g_d / \partial d$ so that:

$$\dot{R} = \int_{\Omega_0} -\frac{\partial g_d}{\partial d} \zeta_d (h)^{\zeta_e} \dot{d} \; dV. \tag{15}$$

The specific choice of g_f has the advantage that h and ψ^{bulk} are equally reduced with growing damage (see Eq. 19). This leads to the most straightforward implementation. Another choice could be proposed to further improve the results but it is not the subject of the current work.

2.2. Balance of mechanical energy

Inserting Eq. (6), (15), (A.2) and (A.11) into Eq. (10), we obtain:

$$\begin{aligned}
&-\int_{\Omega_0} \left(\nabla_0 \cdot \left(g_d \frac{\partial \psi^{bulk}}{\partial \mathbf{F}} \right) + \mathbf{b}_0 \right) \cdot \dot{\mathbf{u}} \; dV + \int_{\partial \Omega_0} \left(g_d \frac{\partial \psi^{bulk}}{\partial \mathbf{F}} \cdot \mathbf{n}_0 - \mathbf{t}_0 \right) \cdot \dot{\mathbf{u}} \; dA \\
&+ \int_{\Omega_0} \left(\frac{\partial g_d}{\partial d} \left(\psi^{bulk} + \zeta_d (h)^{\zeta_e} \right) + \frac{G_c}{l_0 c_0} \frac{\partial w}{\partial d} - G_c l_0 \frac{2}{c_0} \nabla_0^2 d + \kappa \dot{d} \right) \dot{d} \; dV \\
&+ \int_{\partial \Omega_0} G_c l_0 \frac{2}{c_0} \nabla_0 d \cdot \mathbf{n}_0 \dot{d} \; dA + \int_{\Omega_0} \sum_{\alpha=1}^{m} g_d \left(\mathbf{Q}_\alpha + \frac{\partial \psi^{bulk}}{\partial \mathbf{\Phi}_\alpha} \right) : \dot{\mathbf{\Phi}}_\alpha \; dV = 0.
\end{aligned} \tag{16}$$

[4] In other words, the fatigue degradation function g_f is required to prohibit spurious damage growth after $d = 1$ is reached (see Eq. 19).

With Eq. (A.7) and the Neumann boundary conditions:

$$g_d \mathbf{P} \cdot \mathbf{n}_0 = \mathbf{t}_0 \quad \text{and} \quad \nabla_0 d \cdot \mathbf{n}_0 = 0, \tag{17}$$

we extract the governing equation for the displacement field $\mathbf{u}$[5]:

$$\nabla_0 \cdot \left(g_d \frac{\partial \psi^{bulk}}{\partial \mathbf{F}} \right) + \mathbf{b}_0 = 0, \tag{18}$$

and for the phase-field damage field d:

$$\frac{\partial g_d}{\partial d} \left(\psi^{bulk} + \zeta_d(h)^{\zeta_e} \right) + \frac{G_c}{l_0 c_0} \frac{\partial w}{\partial d} - G_c l_0 \frac{2}{c_0} \nabla_0^2 d + \kappa d = 0. \tag{19}$$

We want to point out that Eq. (19) contains, in addition to load history h, a rate-dependent driving force:

$$\begin{aligned} \psi^{bulk} &= \psi^{elas} + \psi^{visc} \\ &= \int \mathbf{P}^{\infty} : \dot{\mathbf{F}} dt + \sum_{\alpha=1} \int \mathbf{Q}_{\alpha} : \dot{\mathbf{F}} dt. \end{aligned} \tag{20}$$

This driving force grows with each load cycle, thanks to its viscoelastic contribution (see Fig. 13). Therefore, fatigue damage can also occur without h (see Fig. 14 and 17 for $\zeta_d = 0$). Although our original model [16] is able to describe fatigue damage due to the viscosity, we incorporate the history variable h to improve the model's agreement with experimental measurements (compare e.g. the red and blue lines in Fig. 17) and to generalize the framework so that it is applicable to rate-independent models.

Eq. (18) and Eq. (19) are transformed into their respective weak form using the standard Galerkin procedure. We discretize the problem in space with linear, plane stress, isoparametric, quadrilateral elements. Details on the numerical implementation can be found in [16].

[5]Since we focus for now on examples that are only exposed to tension loading, we avoid the problem of crack surface contacts and crack growth originating from compressive loading. Therefore, we do not need to split the bulk energy into a positive (tensile) and negative (compression) part, as for example done in [23].

3. Results: Monotonic loading

In this section, we focus on monotonic loading. After presenting our experimental set-ups, we present the identification of the visco-hyperelastic material parameters. Subsequently, we study the influence of the length scale l_0 on the global mechanical response, as well as on the formed damage profile. The following fracture parameter identification considers test configurations in both crack nucleation and propagation. We close the section with the presentation of validation cases.

3.1. Experiments

All experiments are performed on an EPDM rubber with a constant temperature of $20°C$. The displacements are measured using a laser extensometer and we use digital image correlation (DIC) to measure local strain fields.

3.2. Identification of visco-hyperelastic material parameters

The bulk material parameters are identified using uniaxial tensile tests according to ISO 37 with dumbbell specimens and three clamp velocities (see Tab. 1 for the parameters according to Eq. (A.3) and (A.5) and Fig. 9 for the fit).[6]

Table 1: Identified material parameters for the visco-hyperelastic model.

C_1 [MPa]	C_2 [MPa]	C_3 [MPa]
0.8766	0.0705	$1.0763 \cdot 10^{-06}$

β_1 [−]	β_2 [−]	τ_1 [s]	τ_2 [s]
0.1016	0.0071	4.978	449.3

3.3. Influence of the length scale

[33] showed that the combination of the degradation function and crack density function according to Eq. (3) and (9) results in a length scale independent global mechanical response. Since the results in [32] are limited to small strains and linear-elastic materials, we investigate the behavior for large strains and visco-hyperelasticity.

3.3.1. Influence length scale: Uniaxial tension

We perform uniaxial tensile tests (specimen length 20mm and width 4mm, loading rate $\dot{\epsilon} = 0.05$ 1/s) with 2D plane stress finite elements (element size $h^{el} = l_0/8$). To enforce damage nucleation in the center, we apply a Dirichlet boundary condition $d = 0$ at the left and right edge of the sample (see Fig. 4). The fracture material parameters are set to $G_c = 4.5$N/mm and $\kappa = 8 \cdot 10^{-4}$Ns/mm^3, while the fatigue damage parameters are set to zero ($\zeta_d = 0$, $\zeta_e = 0$). We compare the results for length scale $l_0 = 1$mm and $l_0 = 2$mm. The material parameter a is set to $a = 5.0$ for $l_0 = 1$mm and $a = 2.5$ for $l_0 = 2$mm.[7]

Length scale $l_0 = 2$mm results in a wider damage zone (see Fig. 4), but the global force to stretch ratio response is nearly identical (see Fig. 5). We conclude that the model of [33] produces also for finite strains and non-linear material models length scale insensitive global mechanical results.

[6] Cyclically loading rubber, the load on reloading is less than when loading for the first time [24]. This so-called Mullins effect must be especially considered when modeling fracture and fatigue experiments. The used material parameters (Tab. 1) are a compromise between the response for the first loading and the softened response after multiple load cycles. By using the phenomenological model of [24] to incorporate the Mullins effect, the accuracy of our predictions could be increased.

[7] The length scale l_0 is selected large enough (relative to the specimen size) to avoid snap-back behavior. Smaller length scales, for the same specimen dimensions, require path-following methods to solve the model. Possible implementation strategies in the context of phase-field damage models can be found in [29].

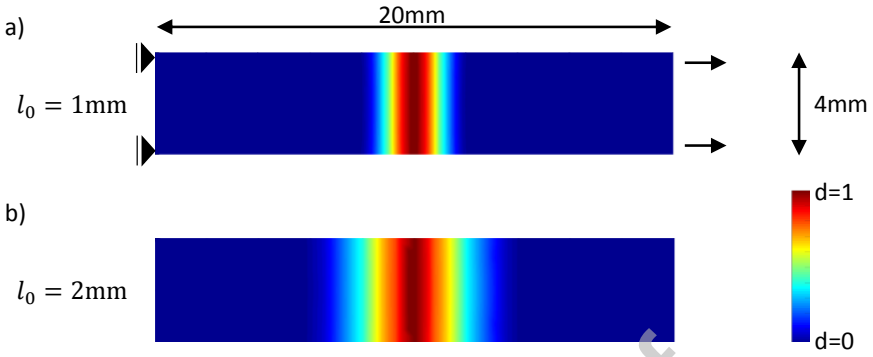

Figure 4: Uniaxial tensile test: Final damage field for a length scale $l_0 = 1.0$mm (a) and $l_0 = 2.0$mm (b). The displacements are applied with a strain rate $\dot{\epsilon} = 0.05$ 1/s.

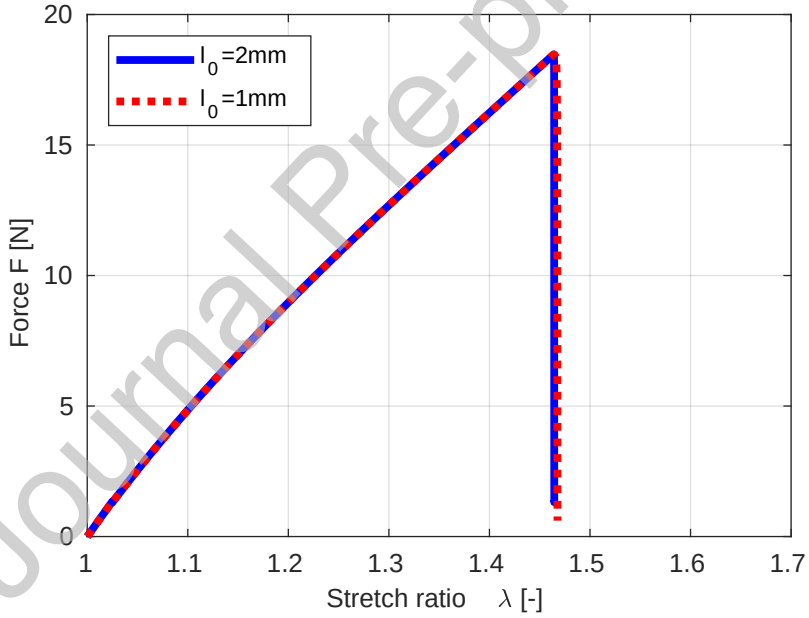

Figure 5: Uniaxial tensile test: Force versus stretch-ratio for a length scale $l_0 = 1.0$mm and $l_0 = 2.0$mm.

3.3.2. Influence length scale: Single edge notched tensile test

In this subsection, we present the results for the SENT tests with an initial crack length of 5mm. The dimensions are depicted in Fig. 6 a), while the fracture material parameters are set to $G_c = 2.0\text{N/mm}$ and $\kappa = 8 \cdot 10^{-4}\text{Ns/mm}^3$ and the fatigue damage parameters are set to zero ($\zeta_d = 0$ and $\zeta_e = 0$). We compare the results for two length scales ($l_0 = 0.25\text{mm}$ and $l_0 = 0.5\text{mm}$). As in Section 3.3, the material parameter a is adapted to ensure that global forces are independent of the length scale parameter. We set $a = 4.0$ for $l_0 = 0.5\text{mm}$ and $a = 8.0$ for $l_0 = 0.25\text{mm}$.

In Fig. 6, we compare the finale damage pattern for the two length scales. The damage process zone is wider for an increasing length scale. In contrast, the maximum tensile strength, as depicted in Fig. 7, remains effectively the same.

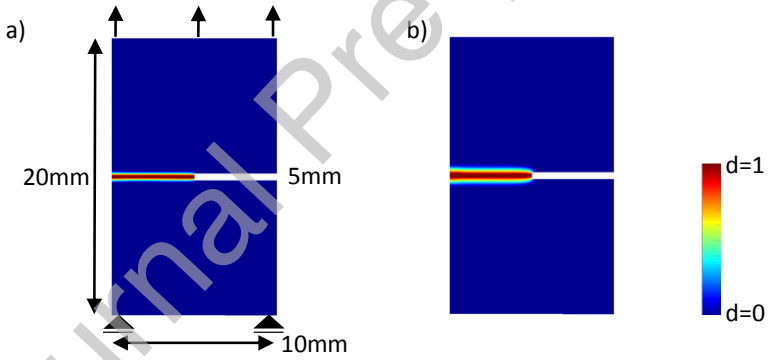

Figure 6: SENT test: Final damage field for a length scale $l_0 = 0.25\text{mm}$ (a) and $l_0 = 0.5\text{mm}$ (b). The displacements are applied with a strain rate $\dot{\epsilon} = 0.05$ 1/s.

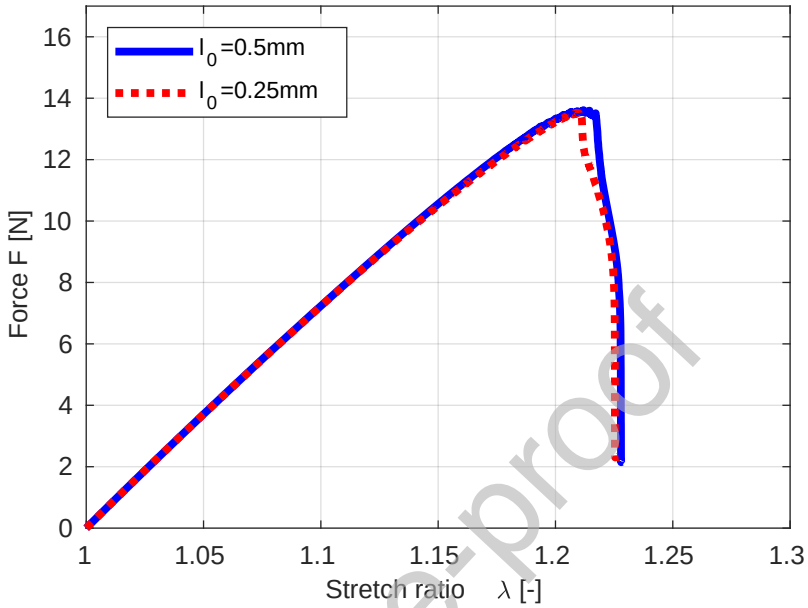

Figure 7: SENT test: Force versus stretch-ratio for a length scale $l_0 = 0.5$mm and $l_0 = 0.25$mm.

3.4. Identification of fracture material parameters

Single edge notch tensile tests (SENT) (see Fig. 8 a) for the dimensions) are performed to identify, together with the uniaxial tensile test, the phase-field fracture parameters. We measure local strains near the crack tip using DIC, but only for a clamp velocity of 25mm/min due to the specifications of the camera. The local strain fields are computed with GOM Correlate software. Fig. 8 b) presents the yy-component of Green's strain tensor at a clamp displacement of 10.5mm (clamp velocity 25mm/min). At this clamp displacement, the crack starts to propagate in our experiments. The phase-field fracture parameters G_c, κ, l_0 and a are identified by minimizing a least squares objective function with

a genetic algorithm:

$$RES = w\Bigg(\sum_{k=1}^{n_{mes25}}\left(\frac{y_{k,25mes}-y_{k,25}}{y_{k,25mes}}\right)^2+\sum_{k=1}^{n_{mes200}}\left(\frac{y_{k,200mes}-y_{k,200}}{y_{k,200mes}}\right)^2 + \sum_{k=1}^{n_{uni,mes}}\left(\frac{y_{k,uni,mes}-y_{k,uni}}{y_{k,uni,mes}}\right)^2\Bigg) + (1-w)\sum_{k=1}^{n_{mes25DIC}}\left(\frac{y_{k,25mesDIC}-y_{k,25DIC}}{y_{k,25mesDIC}}\right)^2, \tag{21}$$

where $w = 0.25$ is a scalar that controls the influence of the force-displacement data relative to the measured strain fields. Subscript mes denotes experimentally measured values. The objective function incorporates the force-displacement data of uniaxial tensile tests $y_{k,uni,mes}$ (strain rate $\dot{\epsilon} = 0.05$ 1/s), the force-displacement measurements of the SENT test ($y_{k,25mes}$ and $y_{k,200mes}$ for clamp velocity 25mm/min and 200mm/min) and the local strain field of the SENT test $y_{k,25mesDIC}$ (clamp velocity 25mm/min).

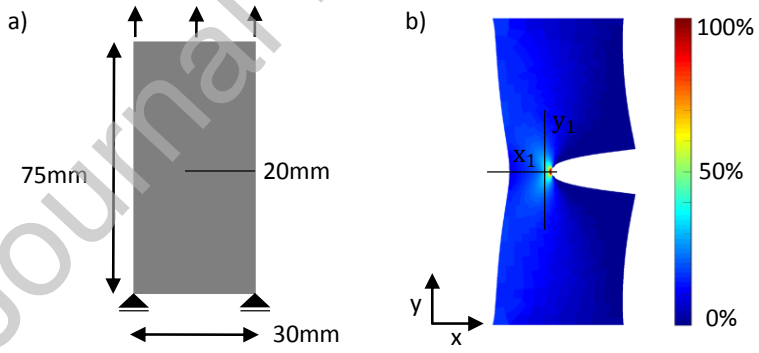

Figure 8: SENT test: a) Specimen dimensions, b) Numerically predicted yy-component of the Green-Lagrange strain tensor at a clamp displacement of 10.5mm. Lines x_1 and y_1 indicate two paths along which we plot strains in Fig. B.22.

This approach diverges from the one presented in [16], since the measurements of double edge notch tensile tests are omitted, and uniaxial tensile tests are included. Tab. 2 presents the identified values, which are used for the following computations. The numerical results for uniaxial tension are presented in the next subsection, while the results for crack propagation are shown in Appendix B. For a more detailed investigation of the rate-dependent fracture of rubbery polymers, we refer to our previous publication [16].

Table 2: Identified phase-field fracture parameters.

G_c [N/mm]	l_0 [mm]	κ [Ns/mm^3]	a [–]
6.0	0.25	0.0192	1.88

3.4.1. Uniaxial tensile test

In this subsection, we show the fitted results of the uniaxial tensile test. The numerically predicted stress-stretch ratio response for the uniaxial tensile test at loading rate $\dot{\epsilon} = 0.05$ 1/s is compared to the experimental ones in Fig. 9. The fit between the numerical and experimental results is satisfactory, including the maximum tearing stress and the maximum stretch ratio.

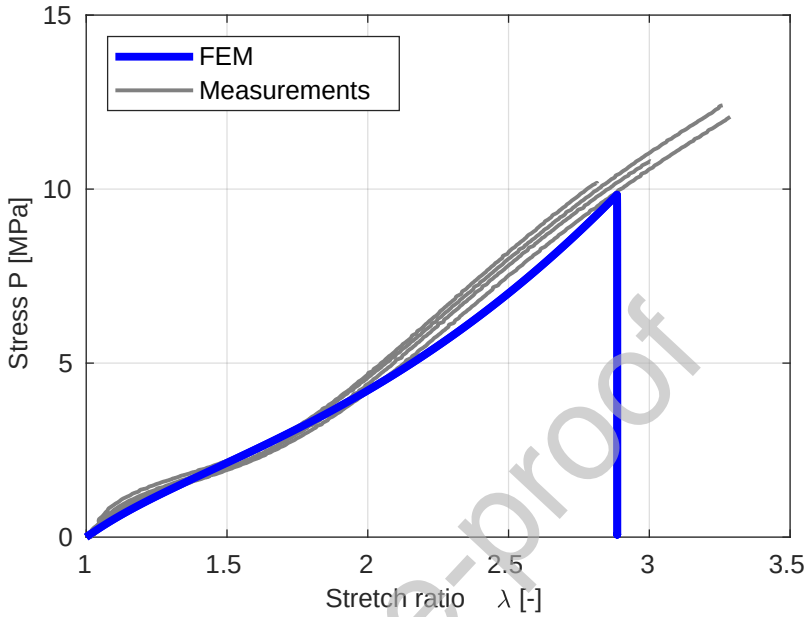

Figure 9: Uniaxial tensile test: Numerically predicted and experimentally observed stress versus stretch-ratio for strain rate $\dot{\epsilon} = 0.05$ 1/s.

3.4.2. Single edge notched tensile test

We validate the identified fracture material parameters (Tab. 2) with simulations of a SENT test according to ISO 34-1 type C. The geometry and the final damage field is presented in Fig. 10, while Fig. 11 presents the match between the experimental and numerical force response. We simulate the test with a fatigue damage source ($\zeta_d = 0.009$ and $\zeta_e = 3$) and without ($\zeta_d = 0$ and $\zeta_e = 0$). The model extension (Section 2.1) for fatigue damage does not influence the results for monotonic loading.

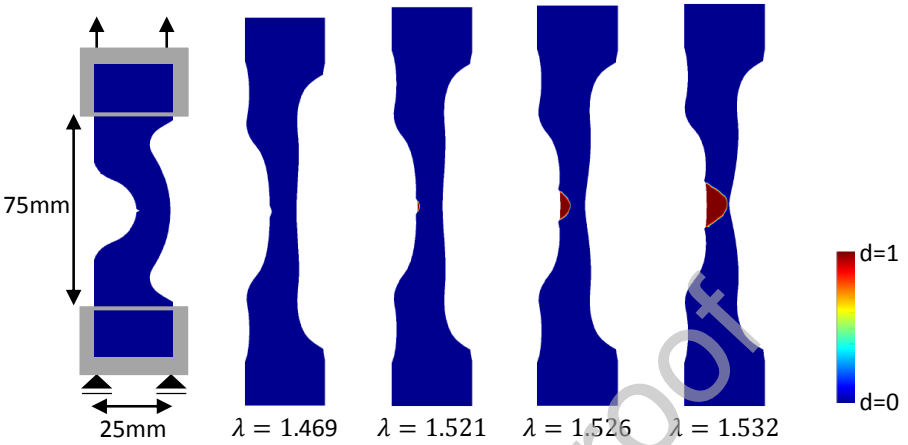

Figure 10: SENT test according to ISO 34-1, type C: Specimen dimensions, boundary conditions (grey) and the damage field for loading rate 200mm/min.

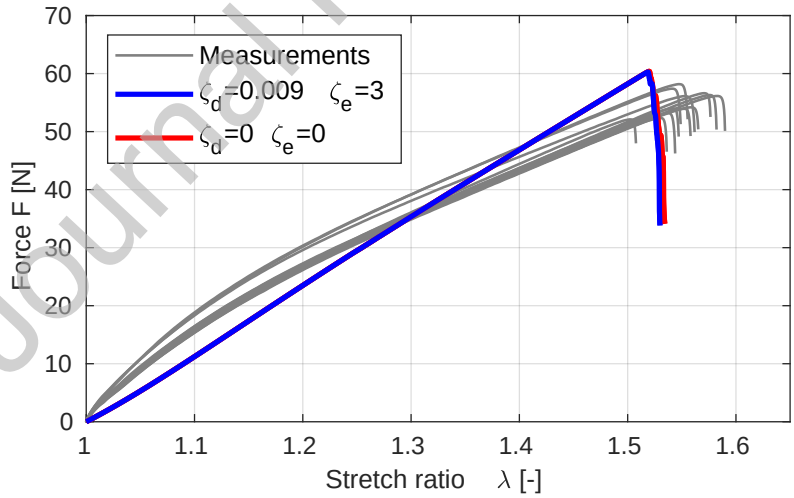

Figure 11: SENT test according to ISO 34-1, type C: Force versus stretch-ratio for loading rate 200mm/min.

4. Results: Cyclic loading

In this section, we shift the focus from monotonic loading to cyclic loading. The thermodynamical consistency of the proposed model is first verified. We perform a parametric study on the influence of the fatigue material parameters, showing the flexibility of the new model to predict fatigue failure independent of the fracture parameters. Subsequently, we study damage growth under cyclic loading for plane stress settings. Fatigue crack growth experiments are conducted with specimens according to ISO 34-1 type C (see Fig. 16). Identifying the fatigue material parameters based on this test, an improved fit with the new model is observed. Finally, we validate our (new) model by extracting the power-law coefficient for fatigue crack growth form pure-shear simulations.

4.1. Uniaxial cyclic tension

4.1.1. Balance of mechanical energy and dissipation during crack growth

Applying uniaxial cyclic tension to a slender bar (length 4mm, width 1mm and thickness 0.25mm), we observe hysteresis in the calculated force versus stretch ratio plot (Fig. 12). If we furthermore visualize the development of the energy of the various model components (with parameters $a = 50$, $\zeta_d = 5$ and $\zeta_e = 1$), it can be observed that the visco-elastically stored and dissipated energy:

$$\psi^{visc} = E^{visc} + D^{visc} = g_d \sum_{\alpha=1}^{m} \int_{\Omega_0} \mathbf{Q}_\alpha : \dot{\mathbf{F}} dt, \tag{22}$$

increases with every load cycle (Fig. 13). We can deduce from Fig. 13 that the model is thermodynamically consistent since the balance of mechanical energy (Eq. 10) is fulfilled at any given time.

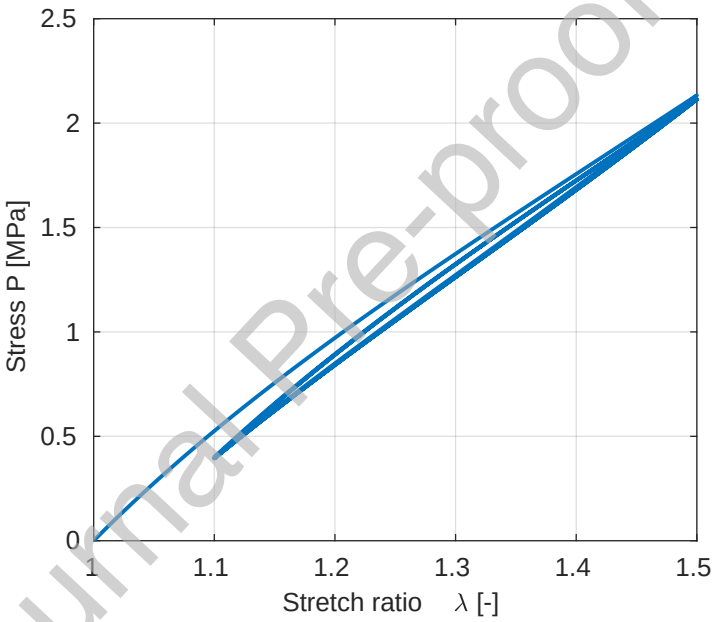

Figure 12: Uniaxial cyclic tension: Stress versus stretch-ratio for strain rate $\dot{\epsilon} = 0.05$ 1/s.

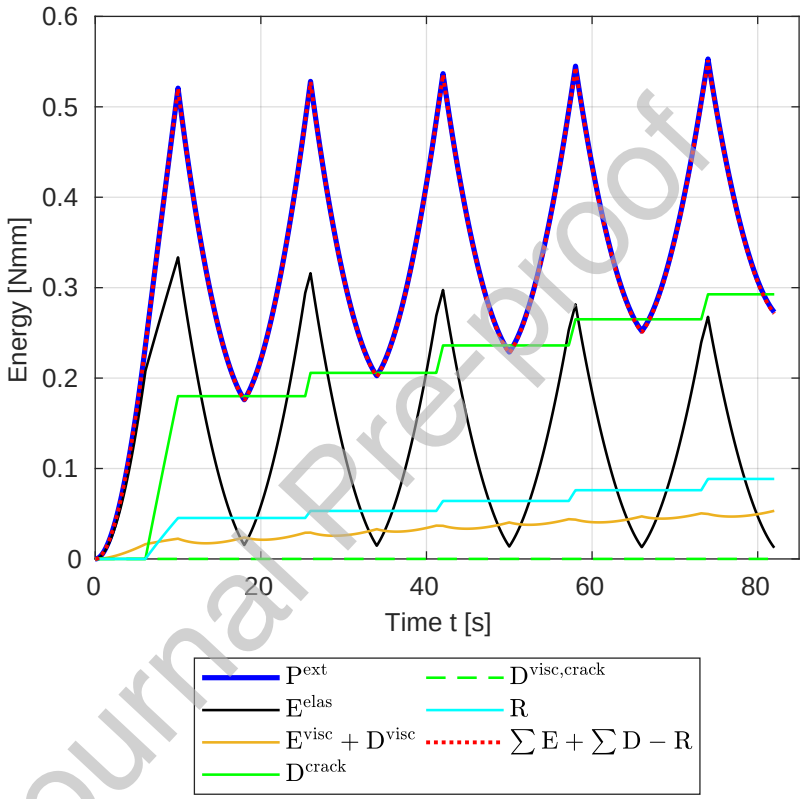

Figure 13: Uniaxial cyclic tension: Energy versus time for the different components of the model. The balance of mechanical energy (Eq. 10) is satisfied for the entire time.

4.1.2. Parametric study: Fatigue damage

Now, we vary the maximum clamp displacement for uniaxial cyclic tension and measure the cycles until failure. The results are presented in Fig. 14 and 15 and so-called Woehler lines are produced. Unloading takes place until 20% of the maximum clamp displacement. Fig. 14 and 15 show that the multiplier (fatigue material parameter ζ_d, Eq. (12)) yields a shift of the response, whilst the exponent (fatigue material parameter ζ_e, Eq. (12)) also yields a slope difference. We conclude from the results that the introduction of the history term with two additional fatigue damage material parameters, leads to a general framework which can be used to fit a desired experimental response (see chapter 4.2).

The parameters ζ_d and ζ_e only affect the result for monotonic loading if both parameters are relatively large (see the response for $\zeta_d = 5$ and $\zeta_e = 1$ at $N = 1$ in Fig. 14). Fig. 14 also shows that if the fatigue damage source is not incorporated ($\zeta_d = 0$), the viscous dissipation in the bulk still yields fatigue damage. The combination of a purely elastic material and a fatigue damage source, for example a load history variable depending on the accumulated strain $h^{elas} = \int (sign(\epsilon_1)\dot{\epsilon}_1)dt$ where $\dot{\epsilon}_1$ denotes the first principle strain, would also lead to fatigue damage. A purely elastic bulk description without a fatigue damage source would however result in an infinite lifetime (assuming failure does not occur in the first cycle).

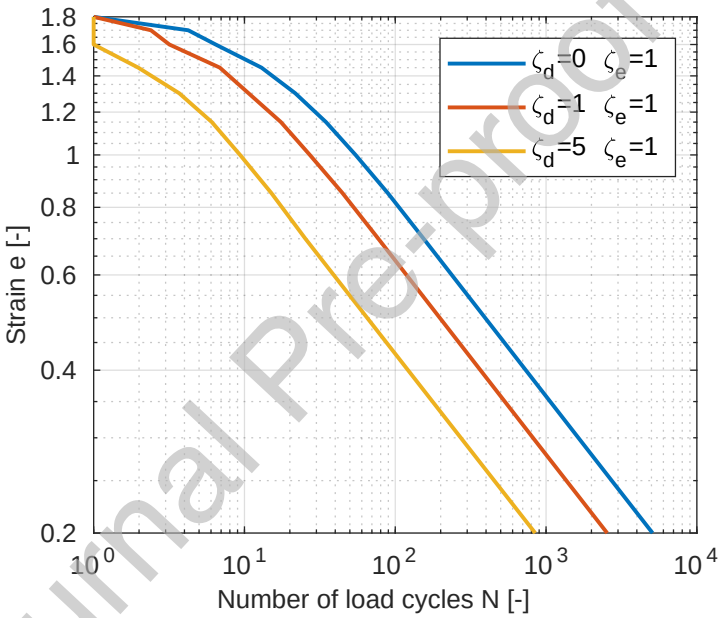

Figure 14: Uniaxial cyclic tension: Strain amplitude versus number of load cycles to failure for different values of multiplier ζ_d.

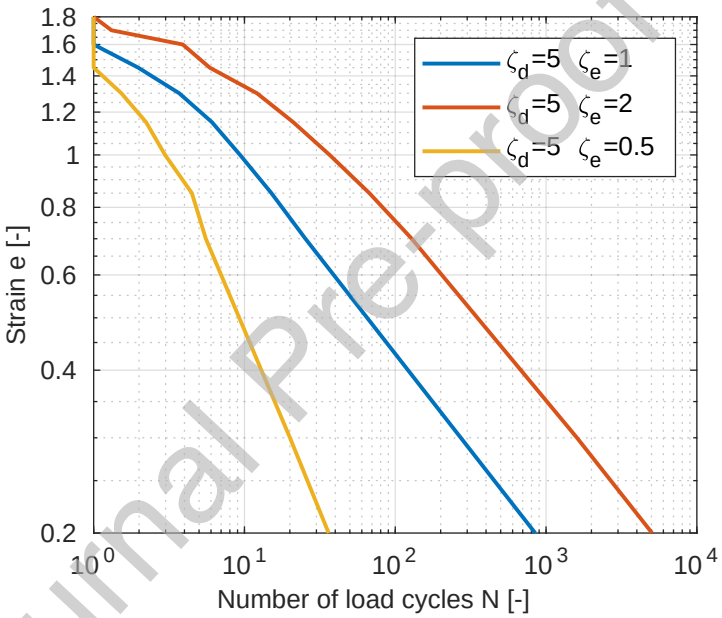

Figure 15: Uniaxial cyclic tension: Strain amplitude versus number of load cycles to failure for different values of exponent ζ_e.

4.2. Single edge notched tensile fatigue test

In this subsection, we focus on single edge notched tensile fatigue tests with specimens according to ISO 34-1 type C (see Fig. 16). We apply a cyclic, displacement controlled load until the sample is totally fractured. During each load cycle, maximum stretch ratio λ_{max} is reached and unloading takes place until $\lambda = 1.075$. The numerically predicted crack is shown in Fig. 16 for $\lambda_{max} = 1.2667$. We use the experimental results of this test to identify the fatigue damage parameters (yielding $\zeta_d = 0.009$ and $\zeta_e = 3$), and compare in Fig. 17 the experimental and numerically predicted lifetime. The match between the measurements and the prediction is adequate. For $\zeta_d = 0$, i.e. no fatigue damage source, the match with the experimental data is inferior, albeit of the same order of magnitude. Since the gap between the experimental lifetime and the calculated lifetime for $\zeta_d = 0$ is constantly increasing for smaller loading amplitudes, the improvement with the new model is visible. [8]

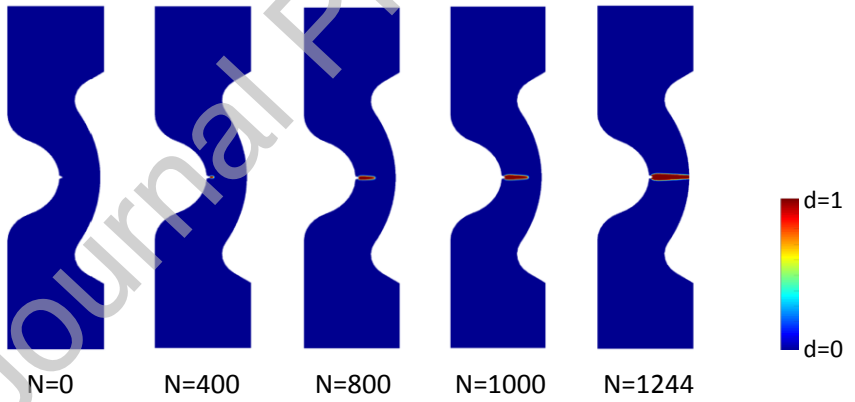

Figure 16: Fatigue SENT test according to ISO 34-1, type C: Numerically predicted damage field ($\lambda_{max} = 1.2667$).

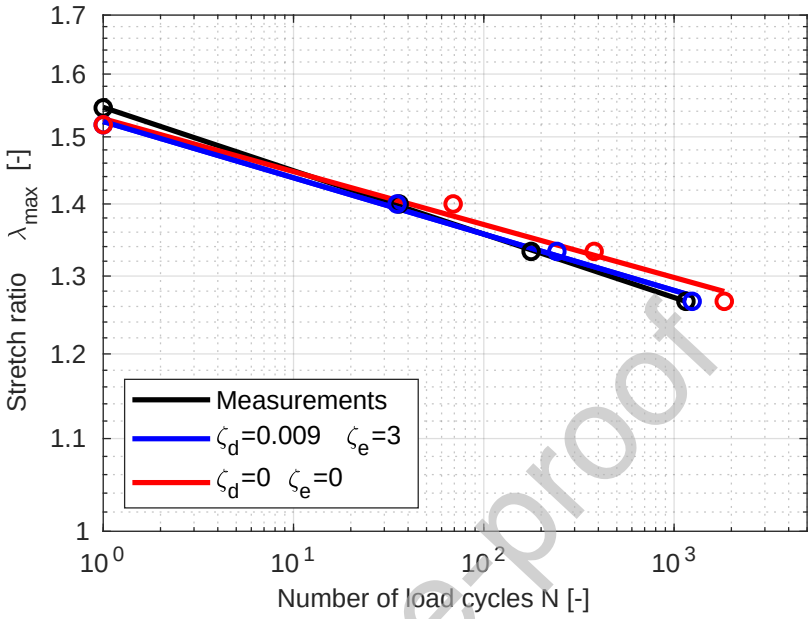

Figure 17: Fatigue SENT test according to ISO 34-1, type C: Numerically predicted and experimentally measured lifetime.

[8]In this contribution we do not consider rate-dependent effects on fatigue damage and perform all cyclic load cases with strain rate $\dot{\epsilon} = 0.05$ 1/s. High loading frequencies can lead to generation of heat, resulting in a change of the material properties and thermal degradation of rubbers [10]. Therefore, experiments are normally conducted so that the temperature rise is only a few degrees and negligible. Nevertheless, [35] found that even for a constant temperature, the loading frequency affects the lifetime of non-crystallizing rubbers like EPDM. [35] observed a decreasing lifetime with a decrease of the frequency and explains this effect with continuous crack growth under static loading. As presented in [16], our model describes this phenomenon and if we increase the frequency of the cyclic loading, we indeed observe a longer lifetime. However, the effect is of a much higher magnitude in our calculations as in [35], which is mainly attributed to a reduced hysteresis of the bulk viscosity. Experiments show a nearly rate-independent hysteresis and [15] proposed to describe this with elasto-plasticity. An extension of the model in terms of plasticity would increase the accuracy of our predictions, but is out of the scope of this publication.

4.3. Pure shear fatigue crack growth

Finally, we present predictions for fatigue crack growth in a pure shear setting. The pure shear specimen is depicted in Fig. 18 and follows ISO 27727. This set-up is characterized by a large width relative to its height. Consequently, the tearing energy G can be calculated independent of the crack length:

$$G = h_o \psi^{elas}. \tag{23}$$

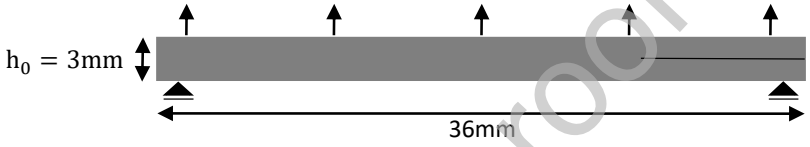

Figure 18: Fatigue pure shear test: Specimen dimensions and boundary conditions. The initial crack length is 9mm.

The simulations are displacement controlled with a minimum strain of 20% of the maximum applied strain.[9] By tracking finite elements with $d > 0.95$, we measure the crack length. In Fig. 19, we plot the current crack length c as a function of the load cycle N for a tearing energy $G = 1.283$N/mm. As expected from the literature (see for example ISO 27727 or [10]) the initial crack growth rate dc/dN is linear.

Performing the simulation for several tearing energies, we can plot the crack growth rate dc/dN as a function of the tearing energy G (Fig. 20). The crack growth of rubber can be described with a power-law relationship between the crack growth rate and the tearing energy:

$$\frac{dc}{dN} = a_1 G^{a_2}, \tag{24}$$

where a_1 and a_2 denote material parameters.

[9]The minimum elongation of 20% of the maximum applied strain ensures that the simplification of disregarding a stress-compression split is valid.

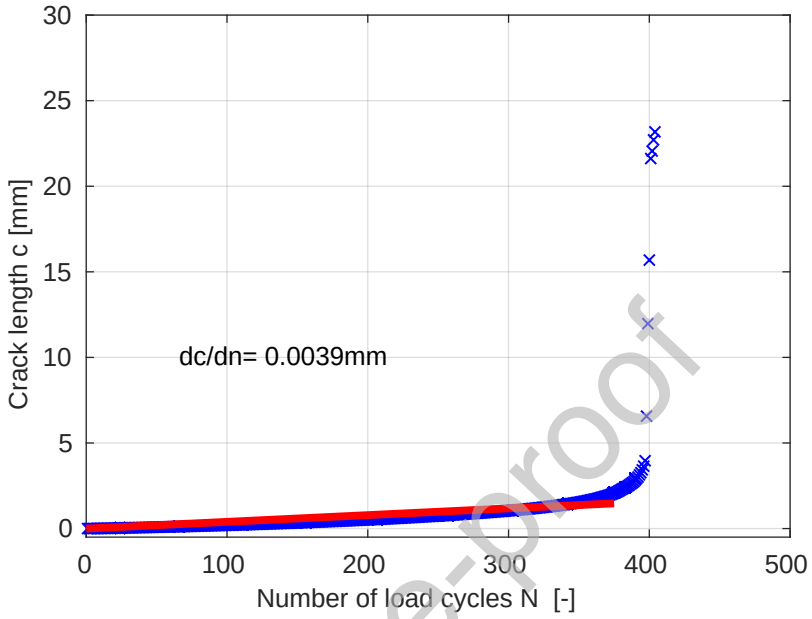

Figure 19: Fatigue pure shear test: Crack length c versus load cycles N for tearing energy $G = 1.283\text{N/mm}$ ($\zeta_d = 0.009$ and $\zeta_e = 3$).

We find $a_1 = 0.0026$ and $a_2 = 1.7188$, which is of the same order of magnitude as reported by other studies (see ISO 27727 ($a_2 = 2 - 6$), [8] ($a_1 = 1.7400 \cdot 10^{-05} - 0.00104$ and $a_2 = 3.19 - 6.05$) or [10] ($a_2 = 2 - 6$)).

4.4. Computational cost

One disadvantage of phase-field damage models is the high computational cost. The model was implemented in MATLAB. Because the code is not parallelized, computing on an Intel Xeon processor at 2.4GHz for a pure-shear test case datapoint (17000 nodes) takes about 24h.

The main reason for the high computational costs is the necessity to calculate each load cycle explicitly. We do not apply a cycle jump technique, but we will examine the acceleration of the computations in the future.

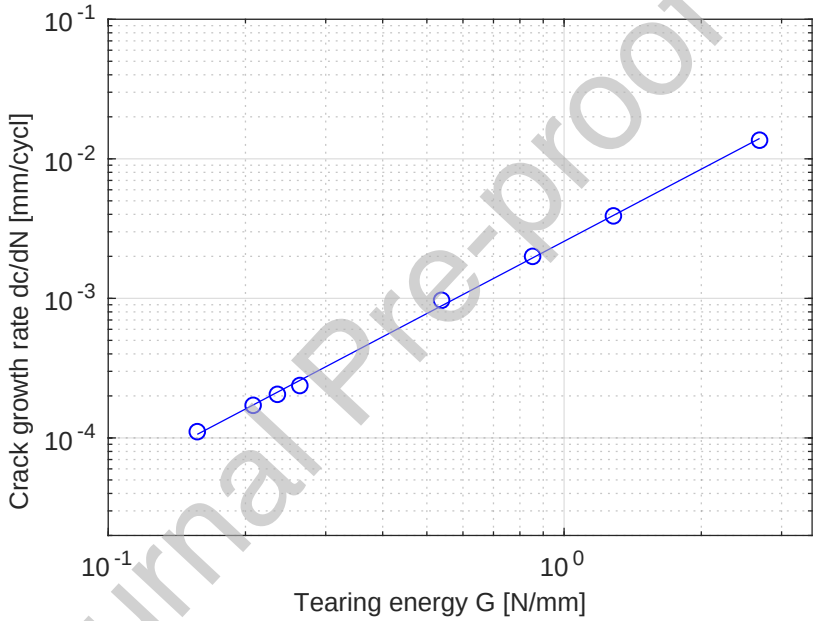

Figure 20: Fatigue pure shear test: Crack growth rate versus tearing energy ($\zeta_d = 0.009$ and $\zeta_e = 3$).

5. Concluding remarks

A rate-dependent fatigue phase-field model for finite strains is proposed based on a load-history dependent fatigue damage source. The general framework allows a flexible choice of the source term and the history variable according to the material being examined. For our rubber, we define the history variable as a function of the dissipation due to the bulk viscosity and introduce two additional fatigue damage material parameters. A reduced polynomial hyperelastic model [34] is used to describe the bulk response, while the rate-dependency of the bulk is incorporated with the well-known material model of [13]. Applying the degradation function and crack density function according to [33], we show global force-displacement results, which are independent of the length scale parameter. All phase-field fracture parameters can be identified from uniaxial tensile tests and single edge notched tensile tests with different clamp velocities. Comparing the results of our predictions with the experimental results, we observe that the model accurately predicts crack nucleation as well as crack growth. The predicted load cycles to failure for a single edge notched tensile test are in good agreement with the experimental ones and the model produces the main characteristic features of fatigue damage, i.e. the Woehler line and the rate of crack growth curve. Future work will focus on the experimental validation for more complex specimens (multiaxial loading) and on accelerating the computations for cyclic loading.

Appendix A. Rate-dependent phase-field damage model

In this appendix, more details on the model components $\dot{E}$, $\dot{D}$ and $\dot{P}^{ext}$ are given.

Appendix A.1. Rate of internally stored energy

The internally stored energy is defined in Eq. 2 with the degradation function $g_d = g_d(d)$ and the strain energy density ψ^{bulk}. The degradation function controls the stiffness of the bulk and requires:

$$\begin{aligned} g_d(d=0) &= 1 \\ g_d(d=1) &= 0 \\ \left.\frac{\partial g_d}{\partial d}\right|_{d=1} &= 0. \end{aligned} \tag{A.1}$$

Most phase-field damage models (e.g. [6], [21] and [22]) use a quadratic degradation function $g_d = (1-d)^2$. In the work of [16] multiple degradation functions are assessed in their performance to match experimental crack propagation data of rubber and the quadratic one performs best. We use the generalized degradation function (Eq. 3) from [32] and [33]. Note that for $a = 2$ the quadratic degradation function is recovered.

The rate of the internally stored energy then reads:

$$\begin{aligned} \dot{E} &= \int_{\Omega_0} \left(g_d \frac{\partial \psi^{bulk}}{\partial \mathbf{F}} : \dot{\mathbf{F}} \right. \\ &+ \left. g_d \sum_{\alpha=1}^{m} \frac{\partial \psi^{bulk}}{\partial \Phi_\alpha} : \dot{\Phi}_\alpha + \frac{\partial g_d}{\partial d} \psi^{bulk} \dot{d} \right) dV, \end{aligned} \tag{A.2}$$

Defining the elastic energy according to [34] :

$$\psi^{elas} = \sum_{i=1}^{3} C_i (tr(\mathbf{F}^T \cdot \mathbf{F}) - 3)^i, \tag{A.3}$$

where C_i are the material parameters, the time-infinity stress reads:

$$\mathbf{P}^{\infty} = \frac{\partial \psi^{elas}}{\partial \mathbf{F}} = 2 \sum_{i=1}^{3} i \; C_i (I_1 - 3)^{(i-1)} \; \mathbf{F}. \tag{A.4}$$

The non-equilibrium stresses are calculated according to [13]:

$$\mathbf{Q}_\alpha = e^{\frac{-\Delta t}{\tau_\alpha}} \mathbf{Q}_{\alpha,n} + e^{\frac{-\Delta t}{2\tau_\alpha}} \beta_\alpha \left(\mathbf{P}^\infty - \mathbf{P}_n^\infty \right), \tag{A.5}$$

where the relaxation times τ_α and scalar free energy factors β_α are the viscoelastic material parameters. Subscript n denotes converged solutions of the previous time step t_n and Δt is the temporal step size. Further details on the viscoelastic material model and its numerical implementation can be found in [13], [14] and [16].

Appendix A.2. Rate of dissipation

The rate of dissipation is attributed to three dissipative phenomena (Eq. 6). According to [13], the rate of dissipation due to the bulk viscosity reads:

$$\dot{D}^{visc} = -g_d \sum_{\alpha=1}^{m} \frac{\partial \psi_\alpha^{vis}}{\partial \mathbf{\Phi}_\alpha} : \dot{\mathbf{\Phi}}_\alpha = g_d \sum_{\alpha=1}^{m} \mathbf{Q}_\alpha : \dot{\mathbf{\Phi}}_\alpha, \tag{A.6}$$

where we have introduced:

$$\frac{\partial \psi_\alpha^{vis}}{\partial \mathbf{\Phi}_\alpha} = -\mathbf{Q}_\alpha. \tag{A.7}$$

The energy dissipated by crack growth is defined in Eq. (8). Note that $w = d^2$ yields $c_0 = 2$, so that the crack density function as defined in [6], [16] and [21] is recovered. By differentiating with respect to time, the dissipation rate due to crack formation can be written as:

$$\dot{D}^{crack} = \int_{\Omega_0} G_c \frac{1}{c_0} \left(\frac{1}{l_0} \frac{\partial w}{\partial d} \dot{d} + 2 l_0 \nabla_0 d \cdot \nabla_0 \dot{d} \right) dV. \tag{A.8}$$

The dissipation rate due to the rate-dependency of the crack growth is defined as:

$$\dot{D}^{crack,visc} = \int_{\Omega_0} \kappa \dot{d}^2 \, dV, \tag{A.9}$$

where scalar κ denotes a viscosity parameter [16].

The second law of thermodynamics requires:

$$\dot{D} = \dot{D}^{visc} + \dot{D}^{crack} + \dot{D}^{crack,visc} \geq 0. \tag{A.10}$$

$\dot{D}^{visc} \geq 0$ is ensured by selecting an appropriate viscoelastic material model [13] (see [14] and [16] for more details). Imposing constraint $\dot{d} \geq 0$ makes the dissipation due to crack growth non-negative ($\dot{D}^{crack} \geq 0$) as well as the dissipation rate due to the rate-dependency of the crack growth ($\dot{D}^{crack,visc} \geq 0$), if $\kappa \geq 0$.

Appendix A.3. Rate of externally applied energy

We denote the surface traction and volumetric body force vector by $\mathbf{t}_0$ and $\mathbf{b}_0$, respectively, so that the rate of externally applied energy reads:

$$\dot{P}^{ext} = \int_{\partial\Omega_0} \mathbf{t}_0 \cdot \dot{\mathbf{u}} \, dA + \int_{\Omega_0} \mathbf{b}_0 \cdot \dot{\mathbf{u}} \, dV. \tag{A.11}$$

Appendix B. Monotonic loading: Results parameter calibration

In this appendix, we present results of the fracture parameter identification tests. The maximum tearing force for clamp velocities of 25mm/min to 200mm/min is successfully predicted (Fig. B.21), as well as the local strain field near the crack tip along paths x_1 and y_1 (see Fig. B.22 and Fig. 8 b) for the definitions of the paths). The correlation between the measured and predicted local strains indicates that the length scale parameter is sufficiently accurately identified. Note that the calibration is only done with the measurements at 25mm/min and 200mm/min, so that the results at $50 - 100$mm/min are true prediction.

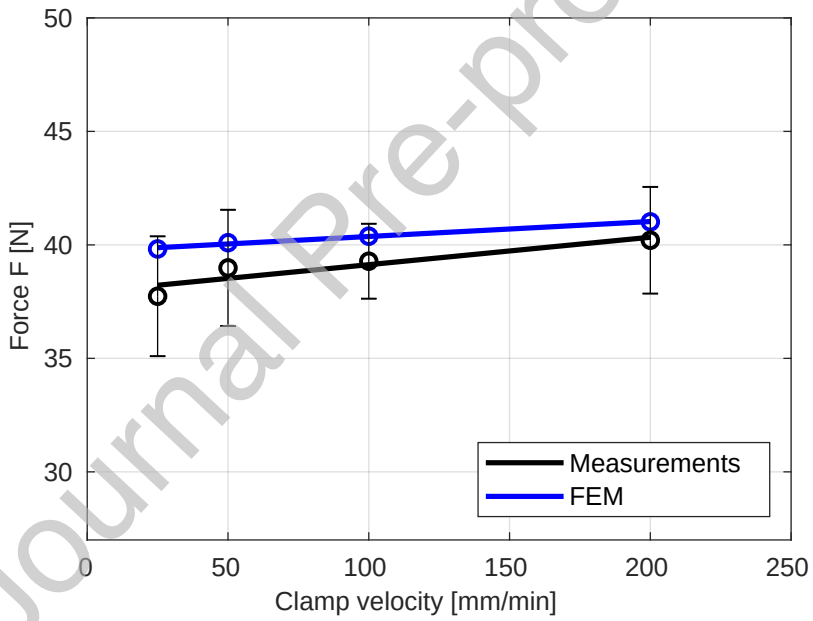

Figure B.21: SENT test: Numerically predicted and experimentally observed maximum tearing force versus clamp velocity.

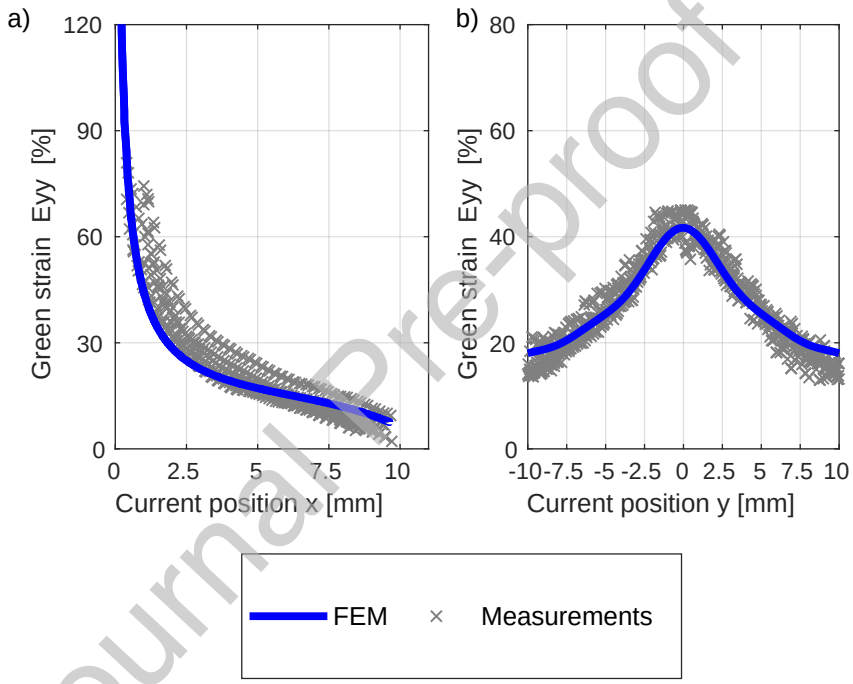

Figure B.22: SENT test: Numerically predicted and experimentally measured yy-component of the Green-Lagrange strain tensor along paths x_1 (a) and y_1 (b) in Fig. 8 b).

Conflict of Interest

Conflict of Interest and Authorship Conformation Form

Please check the following as appropriate

- All authors have participated in (a) conception and design, or analysis and interpretation of the data; (b) drafting the article or revising it critically for important intellectual content; and (c) approval of the final version.
- This manuscript has not been submitted to, nor is under review at, another journal or other publishing venue.
- The authors have no affiliation with any organization with a direct or indirect financial interest in the subject matter discussed in the manuscript

References

References

[1] Abraham, F., Alshuth, T., and Jerrams, S. (2005). The effect of minimum stress and stress amplitude on the fatigue life of non strain crystallising elastomers. *Materials and Design*, 26(3):239–245.

[2] Alessi, R., Vidoli, S., and De Lorenzis, L. (2018). A phenomenological approach to fatigue with a variational phase-field model: The one-dimensional case. *Engineering Fracture Mechanics*, 190:53–73.

[3] Amendola, G., Fabrizio, M., and Golden, J. M. (2016). Thermomechanics of damage and fatigue by a phase field model. *Journal of Thermal Stresses*, 39(5):487–499.

[4] Ayoub, G., Naït-Abdelaziz, M., Zaïri, F., Gloaguen, J. M., and Charrier, P. (2011). A continuum damage model for the high-cycle fatigue life prediction of styrene-butadiene rubber under multiaxial loading. *International Journal of Solids and Structures*, 48(18):2458–2466.

[5] Boldrini, J. L., Barros de Moraes, E. A., Chiarelli, L. R., Fumes, F. G., and Bittencourt, M. L. (2016). A non-isothermal thermodynamically consistent phase field framework for structural damage and fatigue. *Computer Methods in Applied Mechanics and Engineering*, 312:395–427.

[6] Bourdin, B., Francfort, G. A., and Marigo, J. J. (2000). Numerical experiments in revisited brittle fracture. *Journal of the Mechanics and Physics of Solids*, 48(4):797–826.

[7] Caputo, M. and Fabrizio, M. (2015). Damage and fatigue described by a fractional derivative model. *Journal of Computational Physics*, 293:400–408.

[8] Chou, H., Huang, J., and Lin, S. (2007). Effects of Thermal Aging on Fatigue of Carbon Black Reinforced EPDM Rubber. *Journal of Applied Polymer Science*, 103:1244–1251.

[9] de Borst, R. and Verhoosel, C. V. (2016). Gradient damage vs phase-field approaches for fracture: Similarities and differences. *Computer Methods in Applied Mechanics and Engineering*, 312:78–94.

[10] Gent, A. N. (2012). *Engineering with Rubber: How to Design Rubber Components*. Hanser Publishers, third edition.

[11] Guo, Q., Zaïri, F., and Guo, X. (2018). A thermo-viscoelastic-damage constitutive model for cyclically loaded rubbers. Part I: Model formulation and numerical examples. *International Journal of Plasticity*, 101:106–124.

[12] Gurtin, M. E. (1996). Generalized Cahn-Hilliard equations based on a microforce balance. *Physica*, 2003(4):178–192.

[13] Holzapfel, G. A. (1996). On large strain viscoelasticity: continuum formulation and finite element applications to elastomeric structures. *International Journal for Numerical Methods in Engineering*, 39(22):3903–3926.

[14] Holzapfel, G. A. (2001). *Nonlinear solid mechanics: A continuum approach for engineering*. John Wiley & Sons, second edition.

[15] Kaliske, M. and Rothert, H. (1998). Constitutive approach to rate-independent properties of filled elastomers. *International Journal of Solids and Structures*, 35(17):2057–2071.

[16] Loew, P. J., Peters, B., and Beex, L. A. (2019). Rate-dependent phase-field damage modeling of rubber and its experimental parameter identification. *Journal of the Mechanics and Physics of Solids*, 127:266–294.

[17] Marco, Y., Huneau, B., Masquelier, I., Le Saux, V., and Charrier, P. (2017). Prediction of fatigue properties of natural rubber based on the descriptions of the cracks population and of the dissipated energy. *Polymer Testing*, 59:67–74.

[18] Mars, W. (2002). Cracking Energy Density as a Predictor of Fatigue Life Under Multiaxial Conditions. *Rubber Chemistry and Technology*, 75(1):1–17.

[19] Mars, W. and Fatemi, A. (2002). A literature survey on fatigue analysis approaches for rubber. *International Journal of Fatigue*, 24(9):949–961.

[20] Mars, W. and Fatemi, A. (2004). Factors That Affect the Fatigue Life of Rubber. *Journal of Rubber Chemistry and Technology*, 77(3):419–423.

[21] Miehe, C., Hofacker, M., and Welschinger, F. (2010a). A phase field model for rate-independent crack propagation: Robust algorithmic implementation based on operator splits. *Computer Methods in Applied Mechanics and Engineering*, 199(45-48):2765–2778.

[22] Miehe, C. and Schänzel, L. M. (2014). Phase field modeling of fracture in rubbery polymers. Part I: Finite elasticity coupled with brittle failure. *Journal of the Mechanics and Physics of Solids*, 65(1):93–113.

[23] Miehe, C., Welschinger, F., and Hofacker, M. (2010b). Thermodynamically consistent phase-field models of fracture: Variational principles and multi-field FE implementations. *International Journal for Numerical Methods in Engineering*, 83(10):1273–1311.

[24] Ogden, R. W. and Roxburgh, D. G. (1999). A Pseudo-Elastic Model for the Mullins Effect in Filled Rubber. *Proceedings: Mathematical, Physical and Engineering Sciences*, 455(1988):2861–2877.

[25] Ovalle Rodas, C., Zaïri, F., and Naït-Abdelaziz, M. (2014). A finite strain thermo-viscoelastic constitutive model to describe the self-heating in elastomeric materials during low-cycle fatigue. *Journal of the Mechanics and Physics of Solids*, 64(1):396–410.

[26] Pawar, V. S., Guruprasad, P. J., Jha, N. K., Nadella, R., and Nackenhorst, U. (2018). On the constitutive modelling of fatigue damage in rubber-like materials. *International Journal of Solids and Structures*, 159:77–89.

[27] Peerlings, R. H., Brekelmans, W. A., De Borst, R., and Geers, M. G. (2000). Gradient-enhanced damage modelling of high-cycle fatigue. *International Journal for Numerical Methods in Engineering*, 49(12):1547–1569.

[28] Poh, L. H. and Sun, G. (2017). Localizing gradient damage model with decreasing interactions. *International Journal for Numerical Methods in Engineering*, 110(6):503–522.

[29] Singh, N., Verhoosel, C. V., De Borst, R., and Van Brummelen, E. H. (2016). A fracture-controlled path-following technique for phase-field modeling of brittle fracture. *Finite Elements in Analysis and Design*, 113:14–29.

[30] Tanné, E., Li, T., Bourdin, B., Marigo, J. J., and Maurini, C. (2018). Crack nucleation in variational phase-field models of brittle fracture. *Journal of the Mechanics and Physics of Solids*, 110:80–99.

[31] Wang, B., Lu, H., and Kim, G. H. (2002). A damage model for the fatigue life of elastomeric materials. *Mechanics of Materials*, 34(8):475–483.

[32] Wu, J. Y. (2017). A unified phase-field theory for the mechanics of damage and quasi-brittle failure. *Journal of the Mechanics and Physics of Solids*, 103:72–99.

[33] Wu, J.-Y. and Nguyen, P. V. (2018). A length scale insensitive phase-field damage model for brittle fracture. *Journal of the Mechanics and Physics of Solids*, 119(l):20–42.

[34] Yeoh, O. H. (2011). Some Forms of the Strain Energy Function for Rubber. *Rubber Chemistry and Technology*, 66(5):754–771.

[35] Young, D. G. (1985). Dynamic Property and Fatigue Crack Propagation Researchon Tire Sidewall and Model Compounds. *Rubber Chemistry and Technology*, 58(4):785–805.

Author Contribution Statement

Pascal Loew: Conceptualization, Methodology, Software, Validation, Investigation, Writing - Original Draft, Visualization, Project administration, Funding acquisition

Bernhard Peters: Resources, Writing - Review & Editing, Supervision

Lars Beex: Conceptualization, Writing - Review & Editing, Supervision